

Extended morphometric analysis of neuronal cells with Minkowski valuations

Claus Beisbart^{1,2}, Marconi S. Barbosa³, Herbert Wagner² and Luciano da F. Costa³

¹ P.P.M. Research Group

Center for Junior Research Fellows, University of Konstanz, P.O. Box M 682
D-78457 Konstanz, Germany

² Arnold Sommerfeld Center for Theoretical Physics, Ludwig-Maximilians-Universität
Theresienstraße 37
D-80333 München, Germany

³ Cybernetic Vision Research Group, DFI-IFSC
Universidade de São Paulo, São Carlos, SP
Caixa Postal 369, 13560-970, Brasil

Received: date / Revised version: date

Abstract. Minkowski valuations provide a systematic framework for quantifying different aspects of morphology. In this paper we apply vector- and tensor-valued Minkowski valuations to neuronal cells from the cat's retina in order to describe their morphological structure in a comprehensive way. We introduce the framework of Minkowski valuations, discuss their implementation for neuronal cells and show how they can discriminate between cells of different types. codes

PACS. 07.05.Kf Data analysis: algorithms and implementation; data management – 87.19.La Neuroscience – 02.40.Ft Convex sets and geometric inequalities

1 Introduction

Natural phenomena can be understood as causes and consequences of a continuing interplay between geometry and dynamics, or form and function [1,2]. Spatial adjacencies, the specific geometrical features of natural entities, as well as the dimensionality of the space where they are embedded, largely constrain their dynamics and function. For instance, the proper operation of a mammal's heart depends on a suitable diffusion of potentials and waves across the heart surface. It is at the central nervous system, however, that the interplay between form and function reaches its greatest complexity. To begin with, the velocity of signal transmission in neuronal fibers (i.e. dendrites and axons) depends on the width and length of the fibers. The importance of geometry for proper neuronal function is further underlined by the fact that neurons are cells specialized to establish selective connections. Given the spatial constraints imposed by three-dimensional space, these cells have to resort to the most diverse geometries in order to implement the required interconnections – as they do in a dynamical way during the whole lifetime of an individual. As a consequence it is to be expected that morphological analyses of neuronal cells provide clues for understanding neural dynamics and function. Although a large number of investigations have been directed at the neural anatomy and geometry (e.g. [3,4,3,5]), only the taxonomic orga-

nization of neuronal cells or the consideration of shape abnormalities as subsidies for diagnosis have been concentrated on so far. The study of the shape of neuronal cells with objective and mathematically well characterized morphometric descriptors is just at the beginning (e.g. [6, 7, 8, 9]).

In order to be useful tools, such morphological descriptors should fulfill the following criteria: First, the extracted quantitative features should obey simple transformation rules, when the neuronal cell under investigation is subject to elementary geometrical transformations such as affine or conformal transformations (*in-* and *covariance*). Second, the obtained measurements should discriminate between different classes of neuronal cells. Finally, it is important that the estimated features allow for intuitive interpretations from the neuroscience point of view.

Because of their long tradition in modeling and analysis, mathematics, physics and engineering provide a large number of concepts and measures that may be considered for studies in neuroscience and neuromorphometry. A good example is entropy, which has been used in neuroscience because of its close association with the concept of information [10]. Other such measures include the fractal dimension [11,12,13], lacunarity [14,15], percolation critical density [2] and curvature [16]. Recently, concepts from Integral Geometry and in particular the (scalar) Minkowski shape functionals were applied in order to characterize the

geometry of ganglion cells from the cat’s retina [17,18]. Minkowski shape functionals are particularly interesting because they meet the criteria mentioned above: They are invariant under rigid body transformations, seem to have good discriminative power [17], and can be squared with basic concepts from neuroscience. Moreover, they can easily be implemented: Usually, the original data are filtered with methods known from MIA (Morphological Image Analysis). This preprocessing introduces a free parameter, which can later be varied in order to probe the morphology at different scales. In previous works, the singular points (branching and terminating points) [18] or the whole cell outline [17] were dilated, where the dilation radius entered as a parameter. For each dilation radius, the preprocessed neuron image was decomposed into components (or basic building blocks). The Minkowski functionals can then be calculated by counting certain multiplicities of the basic building blocks. This approach makes use of mathematical results from Integral Geometry [19]. In this paper, we use extensions of the Minkowski shape functionals, viz. the *Minkowski valuations*, in order to further improve neuromorphometric characterization and analysis. These extensions were only very recently investigated by mathematicians [20,21,22] and include vector- and tensor-valued measures. They are therefore sensitive to directional information and also allow for valuable graphical visualizations. Minkowski valuations have been successfully applied to describe the morphology of galaxies [23] and galaxy clusters [24].

In the following, we will illustrate the potential of the Minkowski valuations for neuromorphometry by analyzing a set of ten ganglion cells from the cat’s retina. We consider two-dimensional projections of the cells. The set used [25] includes cells with diverse shapes, corresponding to a recently revised classification of those types of cells [26]. In addition, ganglion cells from the retina exhibit branching patterns which are predominantly planar, and therefore compatible with the two-dimensional Minkowski valuations considered in the present work.

The article starts by presenting the higher-order Minkowski functionals and proceeds by illustrating their application to the characterization of neuronal cells.

2 Minkowski valuations

Morphometry deals with measures for the content, shape and connectivity of spatial patterns (“bodies”). Consider a body P in 2-dimensional space such as constituted by the pixels of a neuron image (see Figures 1 and 2 for examples). A straightforward way to measure its “content” is to calculate its area $V_0(P)$ or – equivalently – to count its pixels. The area clearly meets the requirement of motion invariance. Furthermore, it is additive; that is, the area of the set union P of two bodies P_1, P_2 can be decomposed as $V_0(P) = V_0(P_1) + V_0(P_2) - V_0(P_1 \cup P_2)$. Thus, the area can always be calculated by summing up over local contributions from basic building blocks (pixels, e.g.). Finally, the area of a convex body can be continuously approximated by the areas of a sequence of convex polygons (conditional

continuity of V_0).

There are other geometric descriptors that share these properties with the area. The perimeter is a case in point. However, the class of motion-invariant, additive and conditionally continuous descriptors is not unbounded. Let us point this out in full generality for d dimensions. Consider an arbitrary pattern P that can be decomposed into a set union of finitely many convex bodies. According to *Hadwiger’s characterization theorem* [27,28] there are only $(d + 1)$ linearly independent measures $V_0(P), \dots, V_{d+1}(P)$ that obey motion-invariance, additivity and conditional continuity. They are called (*scalar*) *Minkowski functionals*. Thus, in our case of $d = 2$, the area V_0 , the perimeter $4V_1$ and the Euler characteristic V_2 constitute a *complete* family of scalar morphological measures. Note, that the Euler characteristic is a topological invariant and equals the number of connected components minus the number of holes for patterns in \mathbb{R}^2 . The Minkowski functionals were applied to neuronal cell classification in [17,18]. Like the area V_0 , the perimeter V_1 and the Euler characteristic V_2 can be decomposed into local contributions. This time they arise from the boundary ∂P of the body P . For smooth boundaries one has

$$V_1 = \frac{1}{4} \int_{\partial P} d^1 S, \quad V_2 = \frac{1}{2\pi} \int_{\partial P} c d^1 S, \quad (2.1)$$

where c denotes the curvature of ∂P and varies as one moves along ∂P . The factor $\frac{1}{4}$ is a pure matter of convention. For pixel sets, which do not have a smooth boundary, V_1 and V_2 can be calculated by summing up contributions from the bonds that confine the pixels, and the corners, see [19].

A natural way of generalizing the concept of the Minkowski functionals is to replace the requirement of motion *invariance* by motion *covariance*. Motion covariance means that the Minkowski valuations obey simple transformation rules, when the body is moved in space: they transform exactly as vectors or tensors do under transformations of a coordinate system.

The class of motion-covariant, additive and conditionally continuous descriptors can be completely characterized by a generalization of Hadwiger’s theorem [20,29]. It turns out that they can be reconstructed as moments of the Minkowski functionals.

In two dimensions there are three *first-order* moments of the Minkowski functionals, the so-called *Minkowski vectors*. For bodies with a smooth boundary, they can be represented as follows:

$$\mathbf{V}_0 = \int_P \mathbf{x} d^2 A, \quad \mathbf{V}_1 = \frac{1}{4} \int_{\partial P} \mathbf{x} d^1 S \\ \mathbf{V}_2 = \frac{1}{2\pi} \int_{\partial P} c \mathbf{x} d^1 S, \quad (2.2)$$

where \mathbf{x} denotes the position vector of the area (perimeter) element $d^2 A$ ($d^1 S$) to be integrated over. Minkowski vectors can also be defined for pixelized images, which lack a smooth boundary.

For the purposes of our analysis, it will be useful to nor-

malize the Minkowski vectors and to consider the *centroids*:

$$\mathbf{p}_i = \mathbf{V}_i/V_i \quad (i = 0, 1, 2 \text{ if } V_i \neq 0). \quad (2.3)$$

The centroids specify where some aspect of the geometry (area, perimeter, curvature) is concentrated. Note, that the centroids \mathbf{p}_i may, but need not coincide with each other. It can be shown that all centroids coincide for spherically symmetric bodies.

Moving to *second-order moments* yields the *second-rank Minkowski tensors*. They are built upon the symmetric tensor product denoted by $\mathbf{x} \otimes \mathbf{x} =: \mathbf{xx} =: \mathbf{x}^2$. In two dimensions there are more than three tensors, because, for ∂P -integrals, instead of calculating moments with respect to the spatial position \mathbf{x} , one may also consider the local normal \mathbf{n} of the boundary, which points outwards and is normalized to one.¹ Thus, for the integrals $\int_{\partial P} d^1 S$ and $\int_{\partial P} c d^1 S$ three types of second-order weights for building moments are available, viz. $\mathbf{x}^r \mathbf{n}^s$, where $(r, s) = (2, 0)$, $(1, 1)$ and $(0, 2)$ (since we only consider symmetric moments, \mathbf{nx} and \mathbf{xn} are identical). Thus, altogether the following seven tensors can be formed:

$$V_0^{2,0} = \int_P \mathbf{xx} d^2 A, \quad (2.4)$$

$$V_1^{r,s} = \frac{1}{4} \int_{\partial P} \mathbf{x}^r \mathbf{n}^s d^1 S, \quad (2.5)$$

$$V_2^{r,s} = \frac{1}{2\pi} \int_{\partial P} c \mathbf{x}^r \mathbf{n}^s d^1 S. \quad (2.6)$$

In practice, however, we need not consider all of these tensors, because some of them are linearly dependent [21]. It can be shown that only the following tensors carry independent information:

$$V_0^{2,0} = \int_K \mathbf{xx} d^2 A, \quad (2.7)$$

$$V_1^{2,0} = \frac{1}{4} \int_{\partial K} \mathbf{xx} d^1 S, \quad V_1^{0,2} = \frac{1}{4} \int_{\partial K} \mathbf{nn} d^1 S, \quad (2.8)$$

$$V_2^{2,0} = \frac{1}{4} \int_{\partial K} c \mathbf{xx} d^1 S. \quad (2.9)$$

In the following we will concentrate on these tensors. They are listed together with their names in Table 1. The numerics for calculating the Minkowski valuations for pixelized data sets is described in [31].

Because of motion covariance, the numerical values of the second-rank Minkowski tensors depend on the choice of the coordinate system. But in many applications, there is a natural choice for the origin of the coordinate system. For our neuronal cells we will simply take the position of the soma as the origin (in other cases it might be useful to calculate the second-rank Minkowski tensors $V_i^{r,s}$ with respect to the corresponding centroid \mathbf{p}_i for $i = 0, 1, 2$).

In order to illustrate very briefly how the Minkowski valuations work for pixelized data sets, let us consider three

Symbol	Formula	Name
V_0	$\int_P d^2 A$	area
\mathbf{p}_0	$\int_P \mathbf{x} d^2 A / V_0$	center of mass
$V_0^{2,0}$	$\int_P \mathbf{xx} d^2 A$	mass tensor
V_1	$\int_{\partial P} d^1 S$	length of perimeter
\mathbf{p}_1	$\int_{\partial P} \mathbf{x} d^1 S / V_1$	center of perimeter
$V_1^{2,0}$	$\int_{\partial P} \mathbf{xx} d^1 S$	perimeter tensor
$V_1^{0,2}$	$\int_{\partial P} \mathbf{nn} d^1 S$	\mathbf{n} -weighted perimeter tensor
V_2	$\int_{\partial P} c d^1 S$	Euler characteristic
\mathbf{p}_2	$\int_{\partial P} c \mathbf{x} d^1 S / V_2$	curvature centroid
$V_2^{2,0}$	$\int_{\partial P} c \mathbf{xx} d^1 S$	curvature tensor

Table 1. The Minkowski valuations used in this paper.

simple toy examples (some more examples can be found in [31]). They are shown in Figure 1. The red (medium grey) filled square, the blue (dark grey) open square and the green (light grey) \times denote the centroids \mathbf{p}_0 , \mathbf{p}_1 and \mathbf{p}_2 , respectively. The tensors are calculated around the center of the black square in the middle of the pixel sets as origin. The red (medium grey), blue (dark grey) and green (light grey) ellipses within the neurons visualize the tensors $V_0^{2,0}$, $V_1^{2,0}$ and $V_2^{2,0}$, respectively. The ellipse for the tensor $V_1^{0,2}$ is shown at the left-hand side. The equation defining the ellipses is always: $\mathbf{x} = \mathbf{c} + a \left(\frac{\tau_>}{\tau_<} \cos(\phi) \mathbf{e}_> + \sin(\phi) \mathbf{e}_< \right)$, where ϕ runs from 0 to 2π , $\mathbf{e}_>$ ($\mathbf{e}_<$) is the eigenvector corresponding to the larger (smaller) eigenvalue $\tau_>$ ($\tau_<$) of the tensor and \mathbf{c} is the center of the soma (except for $V_1^{0,2}$; its ellipse is shifted to the edge of the panels). So the axis ratios of the ellipses are the ratios of the eigenvalues, and the ellipses point into the direction of the eigenvector with the larger eigenvalue. The size of the ellipses does not carry specific information because of the free scale factor $a > 0$.

In the top panel of Figure 1 the pixel set displays an axial symmetry and is almost point symmetric. Accordingly, the centroids are very close to each other; they fan out along the symmetry axis. The tensors $V_i^{2,0}$ align perpendicular to the symmetry axis, because the whole pixel set is more elongated along the horizontal axis. The tensor ellipses for the mass tensor $V_0^{2,0}$ and the perimeter tensor $V_1^{2,0}$ almost coincide, whereas the ellipse corresponding to $V_2^{2,0}$ is a bit more elongated. The reason is that the corners, which play an important role for the curvature tensor $V_2^{2,0}$ are further away from the middle black square, which only contributes to $V_0^{2,0}$ and $V_1^{2,0}$.

For the middle panel, the figure has been slightly modified: in order to destroy the symmetry, we rearranged one of the “arms”. As a consequence, the average pixel is lower down than in the first panel, so all centroids move downwards. The effect is most prominent for the curvature centroid \mathbf{p}_2 , because it depends on corners, some of which disappear for the rearranged dendrite. Note, furthermore, that the centroids span a non-degenerate triangle, a fact that can be taken as indicating asymmetry. The lack of symmetry is also reflected by the tensor ellipses, which are not parallel any more. Note, furthermore, that the ratios between

¹ First-order moments regarding the normal vectors always vanish, as is shown in [30]

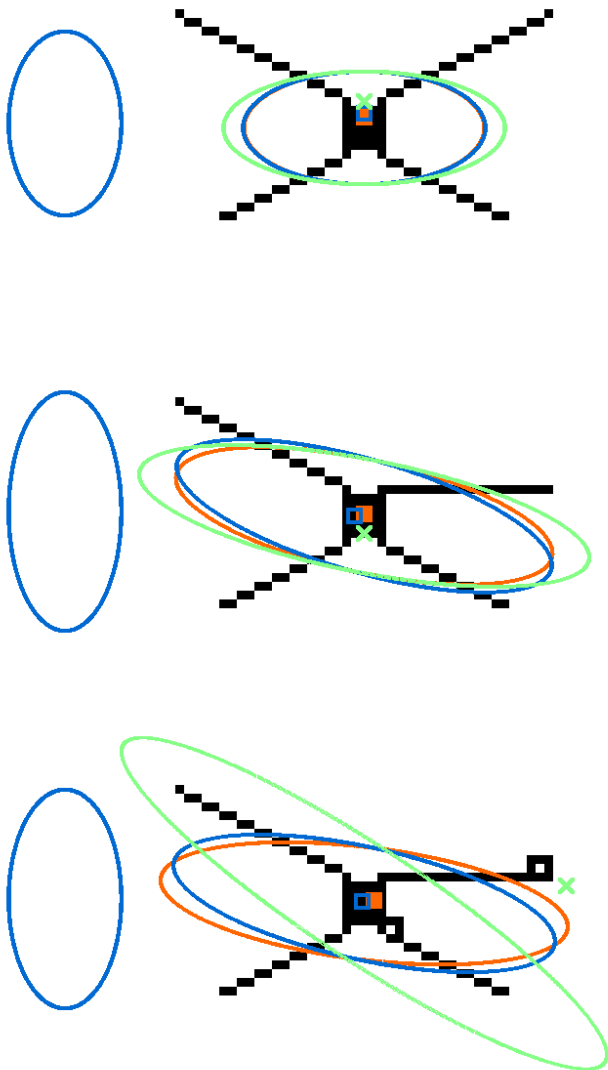


Fig. 1. Three toy examples to be discussed as an illustration. For the centroids the following point styles are used: red (medium grey) filled square: \mathbf{p}_0 ; blue (dark grey) open square: \mathbf{p}_1 ; green (light grey) x: \mathbf{p}_2 . The ellipses carry information about the Minkowski tensors; for more information about the construction of the ellipses see the main text. Red (medium grey) ellipse: $V_0^{2,0}$; blue (dark grey) ellipse: $V_1^{2,0}$; green (light grey) ellipse: $V_2^{2,0}$. Ellipse at the left hand side: $V_1^{0,2}$.

the bigger and the smaller eigenvalues are larger for the second pixel set. The reason is that – due to the “movement” of the upper right arm – the vertical extension of the pixel set shrinks on average, such that the whole body is more elongated.

The bottom panel shows a variation of the body in the middle panel, where two holes have been added. This results in an Euler characteristic of -1 . There is no major effect for both \mathbf{p}_0 and \mathbf{p}_1 and the related tensors. But for \mathbf{p}_2 a big jump can be observed, and the ellipse for the curvature tensor $V_2^{2,0}$ is twisted and more elongated. The

position of \mathbf{p}_2 can be explained as follows: The hole at the right-hand side makes a big negative contribution to \mathbf{V}_2 . So, if \mathbf{V}_2 is calculated around the center of the black square, it points to the left hand side. But since the Euler characteristic V_2 itself is negative, \mathbf{p}_2 is bounced back to the right hand side due to its normalization through V_2 . For the curvature tensor ellipse there is some kind of repulsion from the right hole, because this hole makes a big negative contribution to the tensor; the effect of the other hole is much smaller because it is closer to the soma.

The tensor $V_1^{0,2}$ is shown at the left hand side. It always aligns parallel to the grid axis, the reason for this being that it crucially depends on normals that can only point into four directions for a square lattice.² The shape of the $V_1^{0,2}$ ellipse can be understood as follows: The eigenvalues of $V_1^{0,2}$ count the number of bonds with horizontal or vertical normals, respectively. For all toy examples there are more vertical normals, so the tensor is anisotropic. By moving from the top to the middle panel, more horizontal than vertical normals are destroyed; in this way the tensor becomes even more anisotropic.

Let us conclude this part by adding two comments. First, note, that by considering the eigenvalues of a tensor with respect to an origin which is given by the body itself, motion-invariance is regained. But does this mean that we have been returning to the scalar Minkowski functionals themselves? The answer is no. Additivity has been lost, because forming eigenvalues is not a linear operation, and, as a consequence, the eigenvalues of a Minkowski tensor cannot be decomposed in the same way as the area is. So we have significantly extended the Minkowski framework without having given up its conceptual foundations.

Second, there is a natural extension of our framework to three-dimensional neuron data.

3 The analysis of pixelized neuron data

Data. We analyze two-dimensional neuron data made available by the courtesy of Prof. Berson [25]. We have pixelized maps of ten neurons. They are assigned different types $(\alpha, \beta, \delta, \epsilon, \eta, \iota, \kappa, \lambda, \theta, \zeta)$. The neuron maps greatly differ in terms of scale. Each neuron can be thought of as a subset of filled pixels within a square lattice. Not all of the neuron pixel sets are connected; some of them consist of disconnected parts. This is probably due to an artifact of the neuron observations. We will therefore apply a simple smoothing.

Method. For each cell we construct parallel sets with a ball of radius r_s on a pixel approximation. The parallel set P_{r_s} of a body P comprises all points \mathbf{x} such that the distance between \mathbf{x} and P is r_s at most. The smoothing is illustrated in Figure 2, where the λ -neuron is considered. In the sequel, the smoothing length will be varied and used as a diagnostic parameter. It serves to probe structures at

² For an elementary proof, you can start with a single pixel and then use additivity.

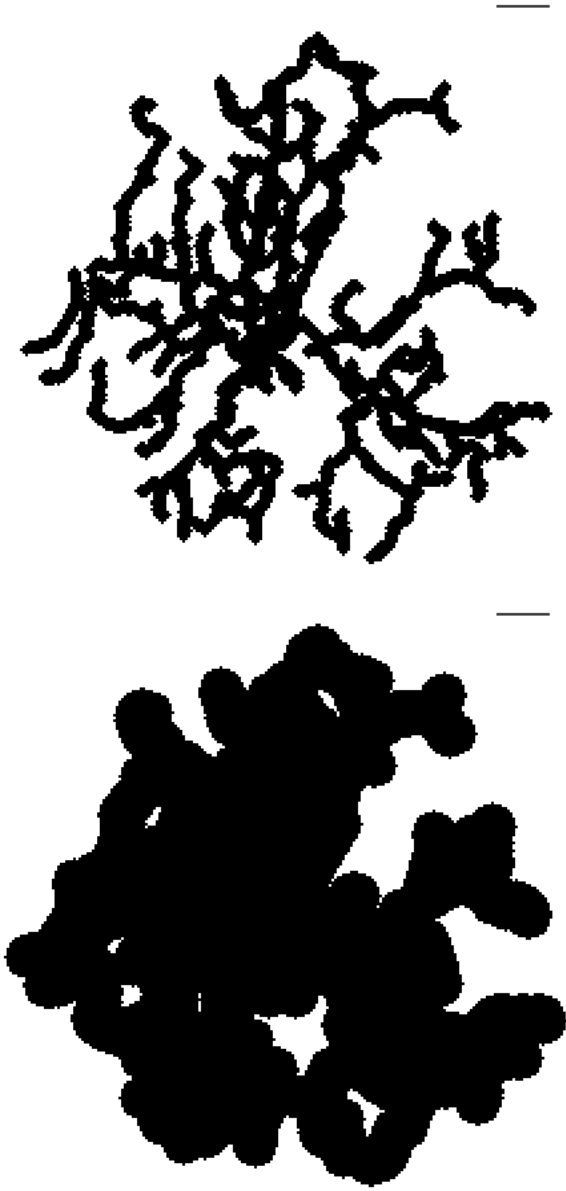


Fig. 2. Two smoothed versions of the λ -neuron. Top panel: smoothing length: 2 pixels. Bottom panel: 8 pixels. The pictures are based on data obtained by [25] (their figure no. 5, copyright permission by Nature Neuroscience).

different scales.

For each neuron that has been smoothed with a particular smoothing length, we calculate the scalar Minkowski functionals, the centroids and the second-rank tensors. For the tensors we choose the center of the soma as a natural origin. The soma and its center are identified visually, in an interactive way.

Results. We show the neurons with some of the results for a smoothing length of one pixel in Figs. 3 – 5.³

³ In the following, one has to be cautious in interpreting the green (light grey) ellipses, because for our neuronal cells, the

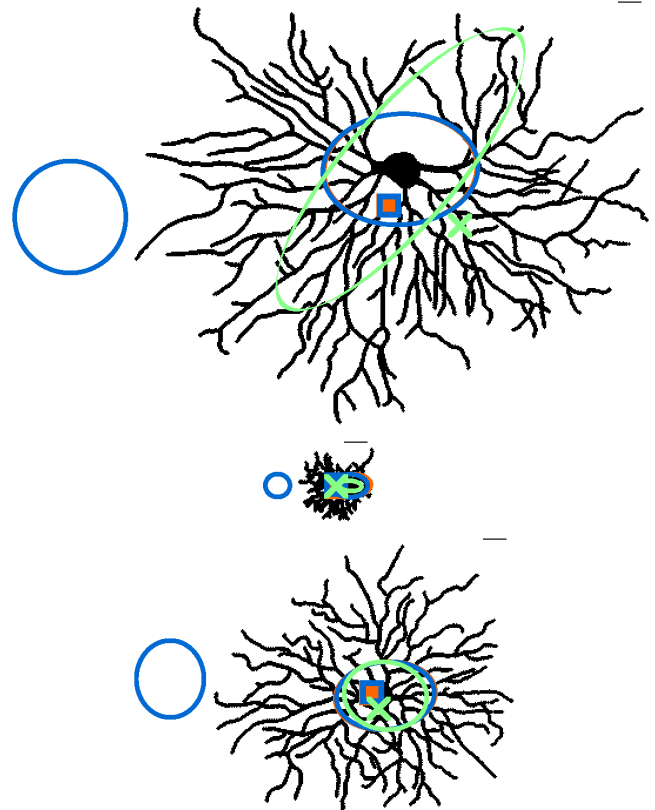


Fig. 3. Neurons of type α (top panel), β (middle panel) and δ (bottom panel). The smoothing length is one pixel. The meaning of the points and the ellipses is explained in Fig. 1. The small dash in the upper right corner of each panel has a length of 20 pixels. The pictures are based on data obtained by [25] (their figure no. 5, copyright permission by Nature Neuroscience). Note, that in all panels of this figure as well as of Figs. 4 and 5 the tensor ellipses for $V_0^{2,0}$ and $V_1^{2,0}$ almost coincide.

Let us start with some qualitative observations. First, the centroids \mathbf{p}_0 through \mathbf{p}_2 are typically not within the soma. Recalling that the centroids are morphological centers, we can equivalently say that the soma is quite often eccentric. It would be interesting to know whether the eccentricity of the soma is characteristic for some types of neurons (for this we would have to investigate larger statistical samples of neurons). We suspect that the eccentricities depend on the function and the local environment of the cells. Further investigations are needed to explore this effect. Second, we observe that typically \mathbf{p}_0 and \mathbf{p}_1 almost coincide, whereas \mathbf{p}_2 may be further away from them. Something similar is true about the tensors: The tensor ellipses of $V_0^{2,0}$ and $V_1^{2,0}$ often closely resemble each other, whereas the ellipse for $V_2^{2,0}$ greatly differs. The reason is as follows: As our toy examples have shown, \mathbf{p}_2 , $V_2^{2,0}$ and the corresponding Minkowski functional (viz. the Euler character-

tensor $V_2^{2,0}$ sometimes has one or two negative eigenvalues. In this case, the ellipse will become smaller and point into the direction of $\mathbf{e}_<$ instead of $\mathbf{e}_>$, if $|\tau_>| < |\tau_<|$.

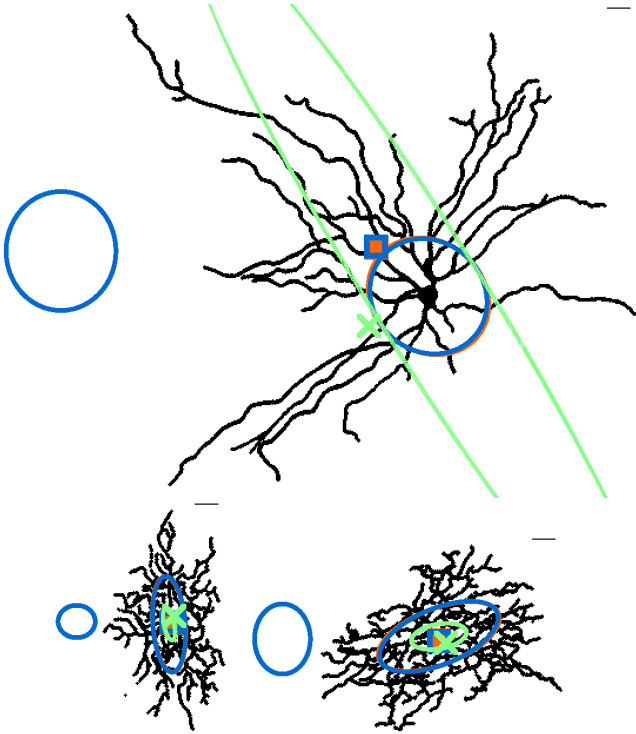


Fig. 4. Neurons of type ϵ (top panel), η (bottom left panel) and ι (bottom right panel). The smoothing length is one pixel. The pictures are based on data obtained by [25] (their figure no. 5, copyright permission by Nature Neuroscience).

istic) are sensitive to holes. For positive Euler characteristics, every hole that is off-soma pushes \mathbf{p}_2 onto the other side of the soma. As a consequence, the location of \mathbf{p}_2 and the form of $V_2^{2,0}$ very much depend on the holes, their forms and positions. The holes in turn depend on tiny details of the branching structure that are not reflected in \mathbf{p}_0 and \mathbf{p}_1 and the corresponding tensors $V_0^{2,0}$ and $V_1^{2,0}$. – Note, that most of the holes are probably due to the projection of the neuron into two dimensions.

We will now turn to a more quantitative analysis. We will show several morphological characteristics that are based upon the Minkowski valuations as a function of smoothing length r_s . The point styles designating the different kinds of neurons are explained in the top panel of Fig. 6.

We show the first scalar Minkowski functional V_0 for a large range of smoothing lengths r_s in the bottom panel of Figure 6. For very small r_s , V_0 grows very quickly, as r_s increases; whereas for larger smoothing lengths, a more moderate growth can be seen. For some neurons it appears to be linear, for other cell types the function $V_0(r_s)$ is clearly convex in this range. Bigger neurons typically grow faster than smaller ones. The explanation is as follows: Let us consider the β cell first. Its overall shape is roughly spherical, and its extension $2r_0$ is about 50 pixels. If the β cell is smoothed with a very large $r_s > r_0 = 25$, all of its substructure is washed out, and we have approximately the same result as if a circle of radius r_0 was smoothed by r_s . So the volume is about $V_0 \approx \pi(r_0 + r_s)^2 =$

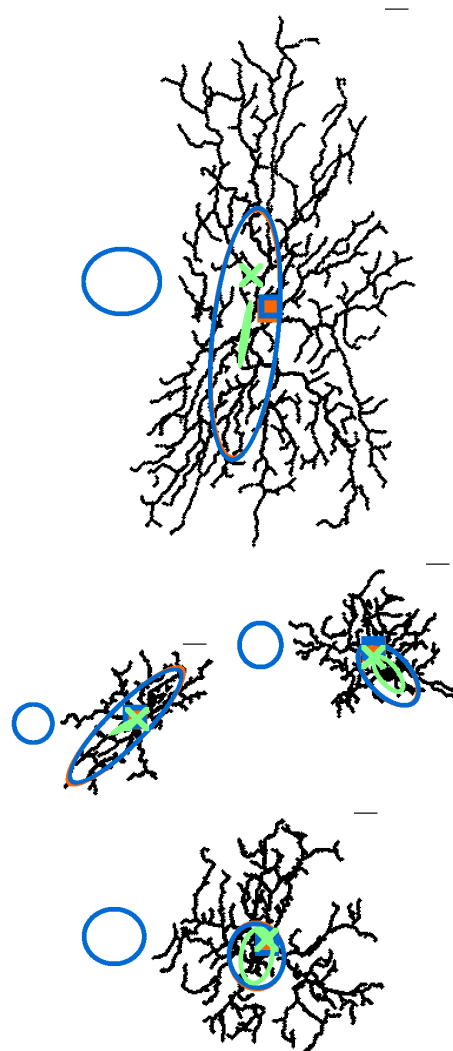


Fig. 5. Neurons of type κ (top panel), ζ (middle left panel), θ (middle right panel) and λ (bottom panel). The smoothing length is one pixel. The pictures are based on data obtained by [25] (their figure no. 5, copyright permission by Nature Neuroscience).

$\pi r_0^2 + 2\pi r_0 r_s + \pi r_s^2$, which is parabolic in r_s . For $r_s < r_0$, the linear term $2\pi r_0 r_s$ is most significant, so the function $V_0(r_s)$ appears to be linear in a certain range.

More generally, let CP denote the convex hull of a pixelized data set P (or, more precisely, the pixel approximation of its convex hull). For large smoothing lengths, the parallel bodies of P and CP , P_{r_s} and CP_{r_s} are very close to each other; consequently the difference $V_0(P_{r_s}) - V_1(CP_{r_s})$ is small compared to $V_0(P_{r_s})$. The size of the parallel body CP_{r_s} can be calculated using *Steiner's formula* (see [28], p. 367, e.g.):

$$V_0(CP_{r_s}) = V_0(CP) + r_s 4V_1(CP) + \pi r_s^2. \quad (3.10)$$

This again defines a parabola, where the Minkowski functionals V_0 and V_1 of CP arise as coefficients. As a consequence, if r_s is large enough, the volume $V_0(P_{r_s})$ is largely determined by the Minkowski functionals of the convex

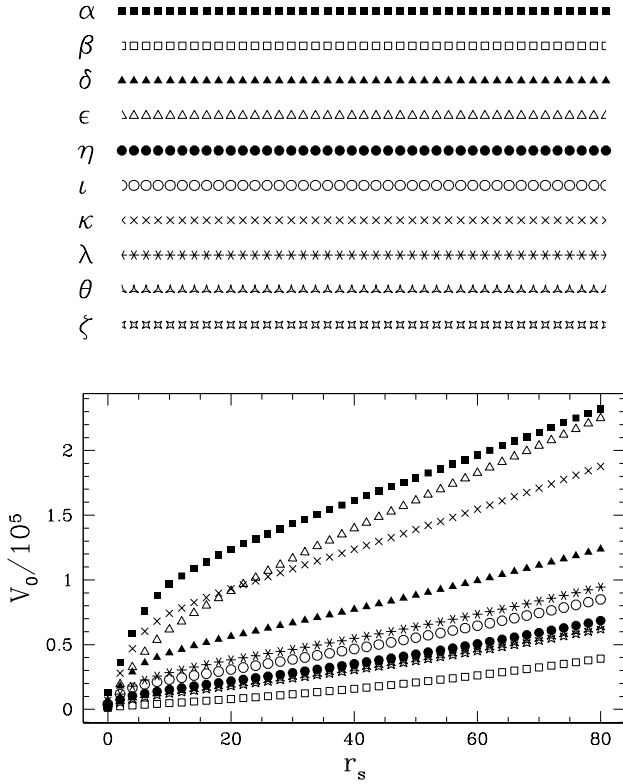


Fig. 6. Top panel: the point styles to be used for the different types of neuronal cells. Bottom panel: the volume V_0 as a function of r_s for a large range of r_s -values.

hull CP . For small neuronal cells such as the β neuron, this behavior sets in quite early. Bigger neurons will have larger values of $V_0(CP)$ and $V_1(CP)$ such that their area V_0 is larger.⁴

In order to observe the fine-grained structure of the cells where the neurons significantly differ from their convex hull, we have to concentrate on smaller smoothing lengths $r_s < 20$. In Figure 7 the scalar Minkowski functionals are plotted vs. the smoothing length r_s . For most neurons, initially, V_0 grows comparatively quickly; around $r_s = 5$, however, the growth slows down. As a reason, the arms of the neurons that have been blown up, when the parallel set was constructed, start to overlap with each other, such that increasing r_s will not necessarily fill many pixels that have not yet been occupied so far.

For some bigger neurons (α , δ , κ , e.g.) a kind of crossover can be observed around $r_s = 5$. For the other types of neuronal cells, the crossover is less pronounced.⁵

We will now consider V_1 . For small r_s , V_1 decreases as a

⁴ Similar considerations apply to V_1 and V_2 .

⁵ Note, by the way, that there are plateaus at the zero points for the V_i vs. r_s curves. More generally, these curves are not continuous, but change stepwise because of our pixelwise smoothing. This can be seen, if the r_s resolution is enhanced. In the following we will neglect discontinuities of this kind; they are a pure artifact of our smoothing and do not carry any physical meaning.

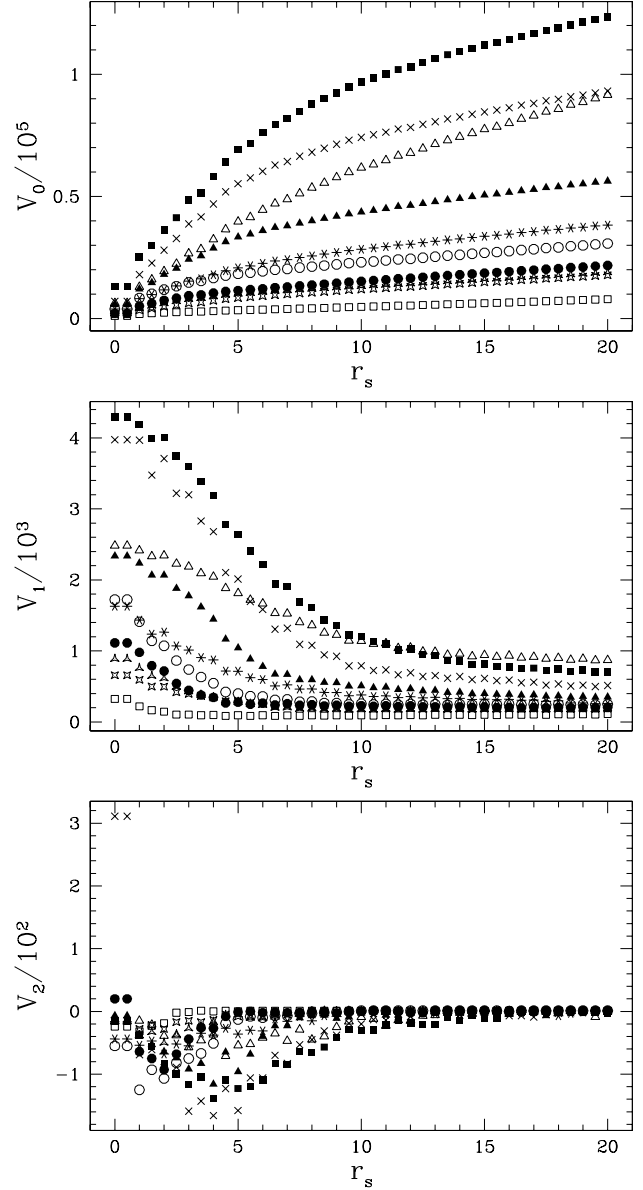


Fig. 7. The scalar Minkowski functionals as a function of the smoothing length for all cells. (Note, that in the first panel the curve for the θ cell is between the curves for the η and ζ types.)

function of r_s , since V_1 is dominated by small scale features that are smoothed away stepwise. V_1 reaches a constant value later on. This is not what one would expect for a convex body. The reason, of course, is that the figure is far from being convex: As r_s increases, V_1 will gain at the outer parts of the cells, but lose in the inner parts, because holes are being filled. Gains and losses roughly compensate each other. Note, that the curves for the α , δ and κ cell type show an inflection point, which very roughly coincides with the position of their crossover in V_0 .

The curves for the Euler characteristic display a number of discontinuities, but there is some more general pattern. The negative values indicate that the cells are dominated

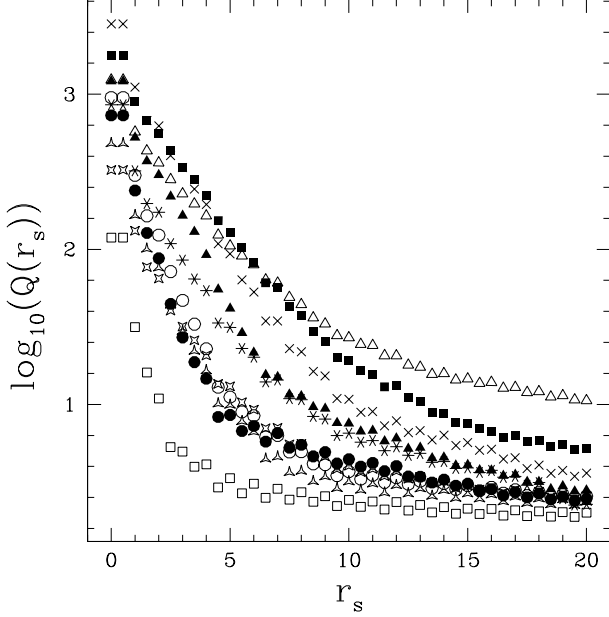


Fig. 8. The logarithm of Q (a variety of the isoperimetric ratio) as a function of r_s .

by holes. For the bigger cell types (α , δ , ϵ and κ) there is a characteristic dip for small r_s . Up to this point, additional holes are formed, as branches of the neuron start to touch each other. The minimum of the dip roughly seems to coincide with the point where V_0 shows the crossover for the bigger neurons. Similar results for the Minkowski functionals have been obtained in [17].

A useful way of combining the information present in the scalar Minkowski functionals is to construct the following dimensionless quantity Q :

$$Q := \frac{4V_1^2}{\pi V_0}. \quad (3.11)$$

This is a variation of the so-called isoperimetric ratio. For a convex body P we have $Q(P) \geq 1$, where the equality holds for a circle [32,33,34]. Q is considerably larger than one, whenever the body under investigation has an “excess perimeter” as compared to its area. We show the logarithm of Q as a function of r_s in Fig. 8. The interpretation is as follows: For small smoothing lengths r_s , most of the dendrites are still present; they produce huge excess areas for which reason Q starts with very high Q -values. As the smoothing length increases, Q goes down. The α , ϵ and κ cells have the largest Q -values, whereas the β -cell has the lowest Q -values for a large range of smoothing lengths because of its smallness and its overall spherical shape. For $r_s < 6$ the decrease in $\log_{10}(Q)$ seems roughly to be linear, where the slopes vary with the cell type.⁶ In Figs. 9 and 10 we consider the centroid distances \mathbf{p}_i -soma, dis_i . For $i = 0$ they are relatively stable as a function of r_s , whereas for $i = 1$ more variation can be observed.

⁶ Note, that “linearity” holds only up to discreteness effects due to our pixelwise smoothing.

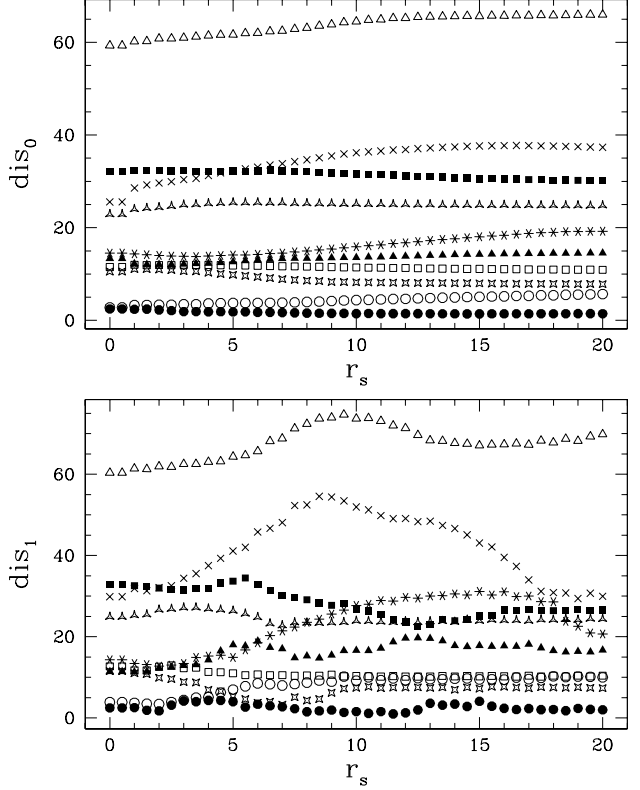


Fig. 9. The distance soma – \mathbf{p}_0 (top panel) and soma – \mathbf{p}_1 (bottom panel) as a function of the smoothing length.

How is this to be explained? Look at the κ neuron as an example (Fig. 5). In the lower half of the image the distribution of small arms is a bit denser than in the upper half. Consequently, for small r_s , there is a significant contribution to the perimeter from this part, and this is also reflected in the position of \mathbf{p}_1 , which is the center of the perimeter. For larger $r_s \approx 10$, however, the lower, denser part is filled more quickly, whereas in the upper part quite big holes are left, which contribute to the perimeter, such that the position of \mathbf{p}_1 moves upwards. In this way the curve for dis_1 contains very detailed information about the morphology of the neuron.

In terms of dis_0 and dis_1 the soma is most eccentric for the ϵ neuron. This is also reflected in our visual impressions. It might be useful, however, to normalize the dis_i parameters by some estimate of the cell size. If we would do so, smaller cells would have a reasonable chance of having bigger eccentricities.

For $i = 2$ (Fig. 10) we observe even larger variations of the centroid distances. Plateaus alternate with jumps that can ultimately be traced back to discontinuities of the Euler characteristic. For small neurons, such as the β type, however, there is not much variation, because the cell is very small and gets completely filled pretty soon. For the α , δ and ϵ -type, there is a common pattern: As the smoothing length increases, the jumps become larger. The reason is probably, that for larger smoothing lengths only a few holes will appear far off centered. When one of these outer holes disappears, \mathbf{p}_2 jumps considerably.

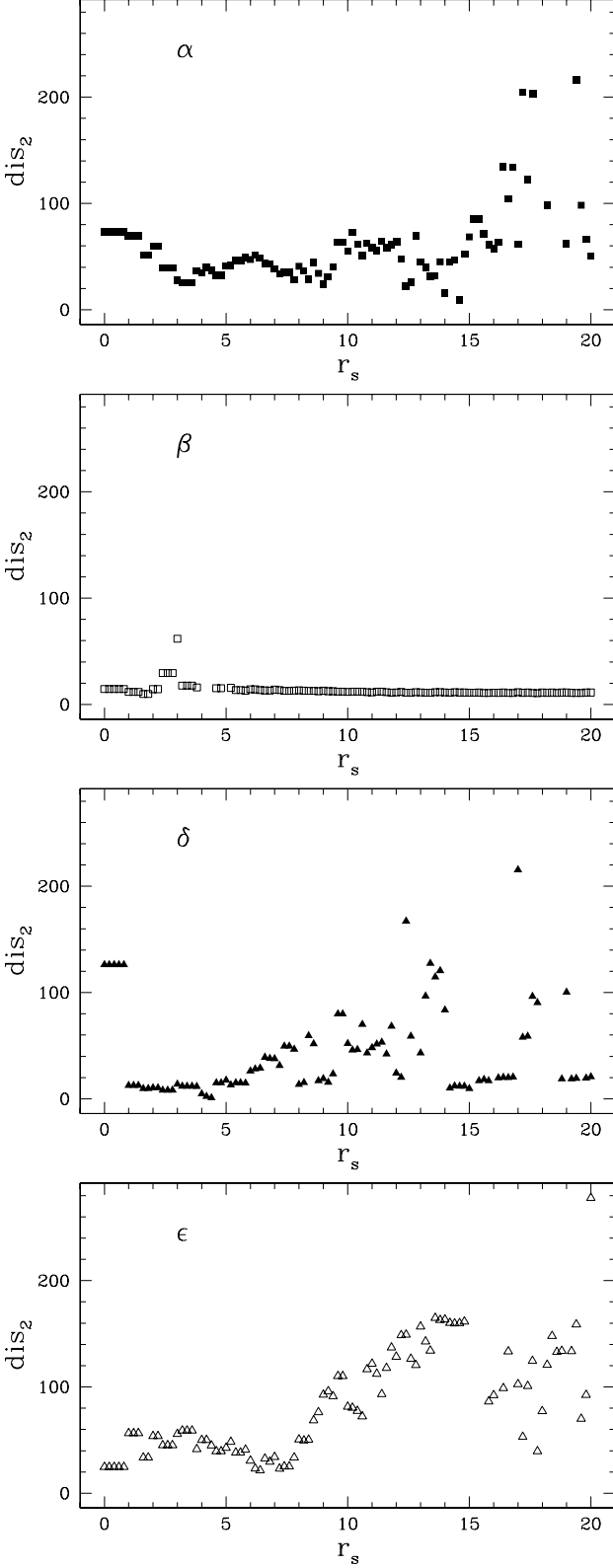


Fig. 10. The distances soma – \mathbf{p}_2 as a function of the smoothing length for four cells. If \mathbf{p}_2 is not defined for some r_s (because of $V_2 = 0$), no point is shown.

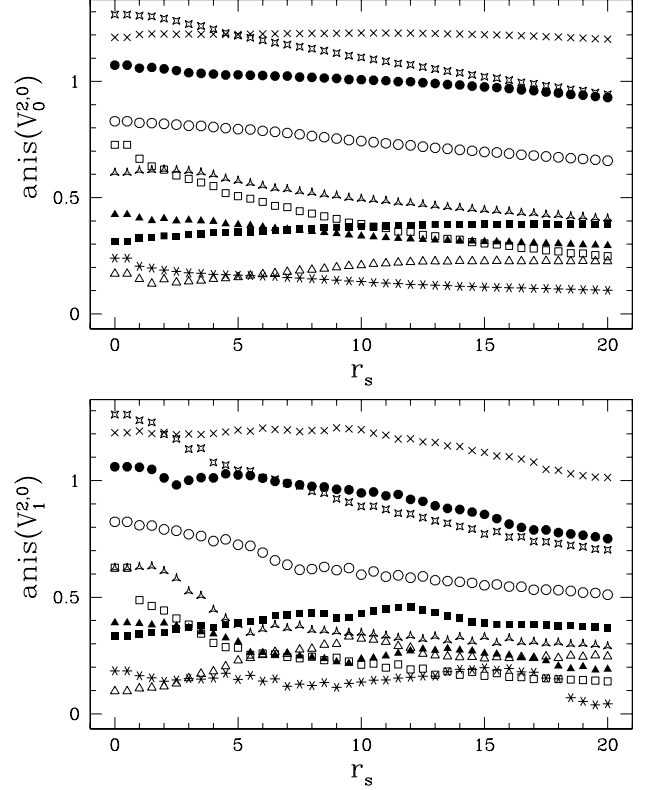


Fig. 11. The anisotropy parameters derived from the mass tensor $V_0^{2,0}$ (top panel) and the perimeter tensor $V_1^{2,0}$ (bottom panel) as a function of the smoothing length.

In Figures 11 through 13 we consider the anisotropy of the cells. In order to quantify anisotropy we take the eigenvalues of the tensors $V_i^{j,k}$, $\tau_>$ and $\tau_<$ and calculate the quantity $anis := 2(\tau_> - \tau_<)/(|\tau_>| + |\tau_<|) \leq 2$. The anisotropy parameters derived from different tensors focus on different kinds of anisotropy (the area elements belonging to a body might be distributed differently from those of its perimeter elements, for instance). As can be seen from Fig. 11, the anisotropies in $V_0^{2,0}$ and $V_1^{2,0}$ are quite stable; most often they decrease slowly, as the smoothing length increases. This indicates that the cells display large-scale anisotropies that are not destroyed by smoothing the cell. For some cells (η , κ , ζ) the anisotropies are considerable. For each cell type the anisotropies of area and perimeter do not differ greatly. The $V_1^{2,0}$ tensor is a bit more sensitive to small-scale variations of the morphology, however; so the $anis(V_1^{2,0})-r_s$ curves appear less smooth than the $anis(V_0^{2,0})-r_s$ curves. On the other hand, across the range of cell types, the variation is quite high. Thus anisotropies seem to have a significant discriminative power.

It is different with the tensor $V_2^{2,0}$, which is considered in Figure 12. The anisotropy derived from this tensor jumps back and forth and sometimes reaches values that exceed those derived from the other tensors. This performance should not come as a surprise, since we have already seen that other characteristics that are related to the Euler characteristic such as $V_2^{2,0}$ typically show discontinuities.

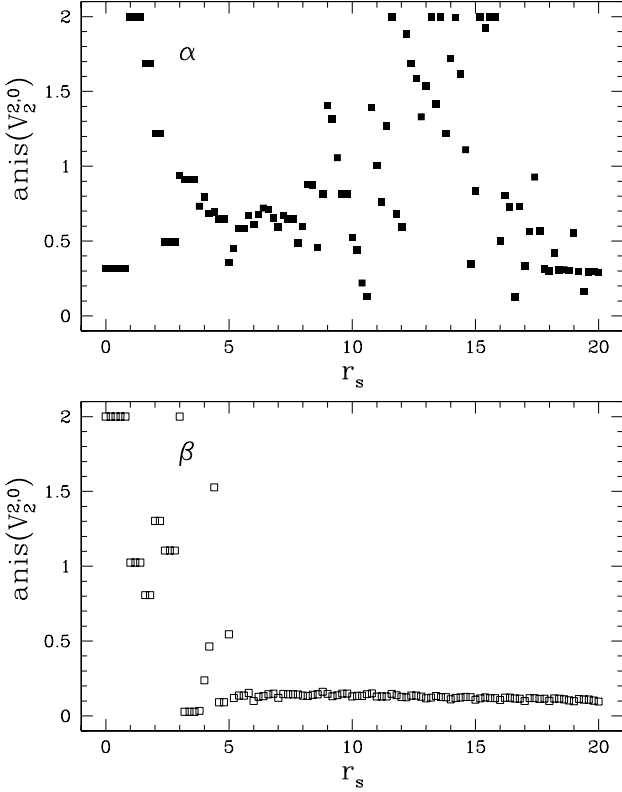


Fig. 12. Another anisotropy parameter (derived from $V_2^{2,0}$) for two cells as a function of the smoothing length.

At some point, however, when the smoothing has produced one connected pattern without holes (visible for the β cell, e.g., where this point is reached quite early), the anisotropy stabilizes at a constant value. Apart from this, the dependence on r_s looks rather chaotic; so far, we are not able to extract information that might help to discriminate between the different cell types.

As mentioned before, on the square lattice, the last tensor to be considered, $V_1^{0,2}$, has a simple interpretation. It checks whether the majority of normals are parallel to the horizontal or to the vertical grid axis. If ∂P is dominated by vertical or horizontal normals, $V_1^{0,2}$ will display a corresponding anisotropy; if not, $V_1^{0,2}$ will roughly be isotropic. In Figure 13 we show some results for single neurons. One can learn from this that the anisotropies arising from $V_1^{0,2}$ are quite small. The anisotropy is comparatively large for the η type cell, because this cell is clearly elongated. For small values of the smoothing length, $\text{anis}(V_1^{0,2})$ is not so much influenced by the overall shape of the neuron, but rather by the directions of the single arms. Interestingly, the graphs shown are qualitatively different for the different types of cells: One cell (viz. the α cell) starts with zero anisotropy, whereas others begin with a non-zero anisotropy. Moreover, there are significant peak structures. But because of its relation to normals, \mathbf{n} , the value of $V_1^{0,2}$ depends to a large extent on the orientation of the cell with respect to the grid. For this reason $V_1^{0,2}$ is only of limited use.

In Fig. 14, the *traces* of the tensors $V_i^{2,0}$ are considered (the trace of the fourth tensor, $V_1^{0,2}$ need not to be taken into account at this point, because it equals V_1). Qualitatively, the viewgraphs for $V_i^{2,0}$ resemble the curves of their scalar counterparts, V_i for $i = 0, \dots, 2$. In order to extract more specific information, it is thus useful to divide $\text{Tr}(V_i^{2,0})$ by V_i , respectively, for $i = 0, \dots, 2$. The result is a measure of how concentrated a cell is in terms of area, perimeter or curvature: $\text{Tr}(V_0^{2,0})/V_0$, for instance will be the bigger, the further the soma and those parts of the cell that bear most of its volume lie apart. Results can be seen from Figure 15. $\text{Tr}(V_0^{2,0})/V_0$ increases continuously, as r_s is enhanced. The reason is that more and more pixels are added at the outer parts of the neuron, so the neuron becomes less and less concentrated. In $\text{Tr}(V_1^{2,0})/V_1$ there is a kink at least for some neurons ($\alpha, \delta, \epsilon, \kappa$). It indicates an additional growth effect. Very probably the explanation is that for small r_s , the small branches within the cell significantly contribute to $V_1^{2,0}$, so the neuron appears to be very concentrated; for larger values of r_s the arms merge and do not contribute to the perimeter any more, so most of the neuron's perimeter is found at its outer parts. Note, that the kinks roughly set in at the r_s -locations of the crossover point in V_0 and the inflection point in V_1 for the α, δ and κ cells.

Constructing global measures A multiscale analysis like that presented in this paper, leads to rich and detailed information on the geometrical aspects of an object. Nevertheless, once such a description of the data has been obtained, it is often useful to derive a compact set of global measures that summarize the most important morphological aspects. In this paper, we consider several ways of condensing multiscale information, i.e. a function of some scale, into simple parameters: The *monotonicity index* [17, 18] is defined as

$$i_s = \frac{s}{s + d + p}, \quad (3.12)$$

where s , d and p count each time the function increases, decreases and remains unchanged, respectively. Thus i_s quantifies the fraction of the interval where the function is monotonically increasing. The *mean value* is the average value of the function over the interval. The *half scale* is the scale at which the area below a curve reaches half of its total value. A different way of constructing global parameters is to consider the *slope* of some characteristic in some particular range of r_s -values.

In Figure 16 we visualize the average slopes of V_0 in the range $r_s \in [10, 60]$ and of $\log_{10}(Q)$ in the range $r_s \in [1.5, 4.5]$ for the different cells. In both cases we choose a range of r_s -values for which the functionals under investigation look roughly linear for most cell types. Results are shown in Figure 16. One can immediately see that the slopes discriminate amongst the different cell types.

In order to further illustrate our approach, we selected two two-dimensional feature spaces, which are spanned by

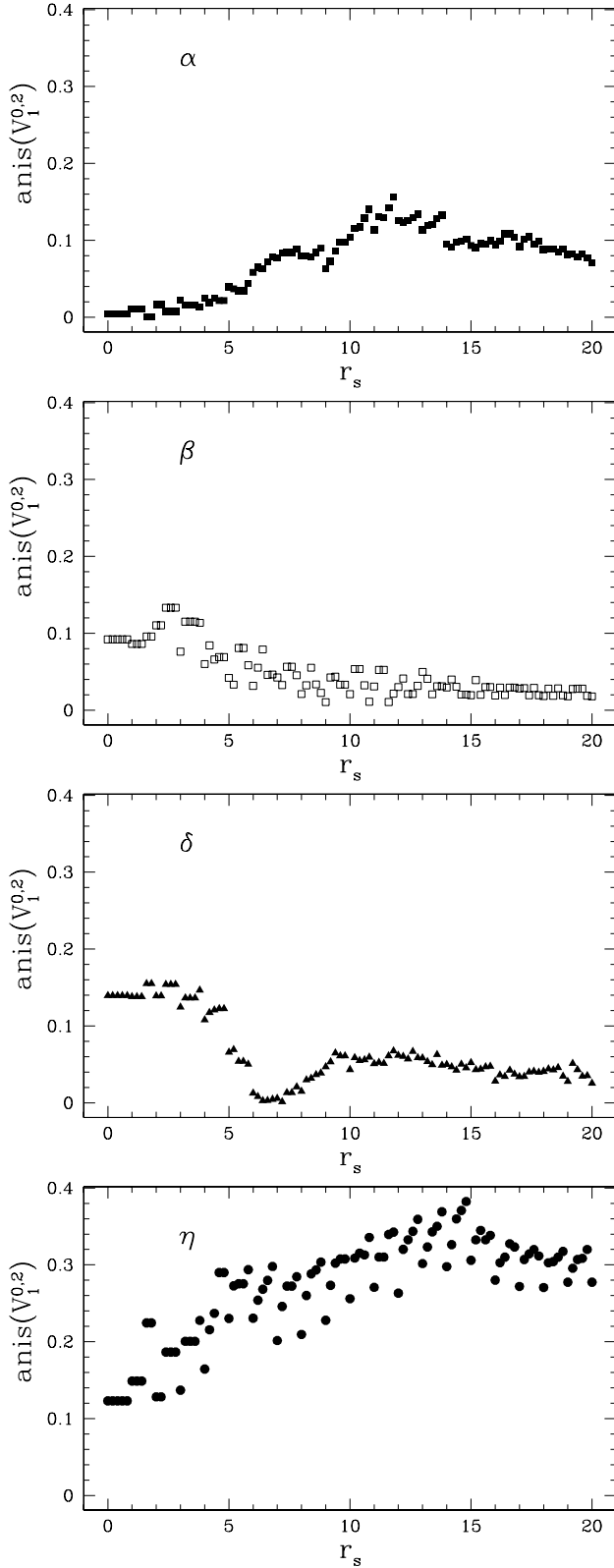


Fig. 13. The anisotropy parameter derived from $V_1^{0,2}$ for four cells as a function of the smoothing length.

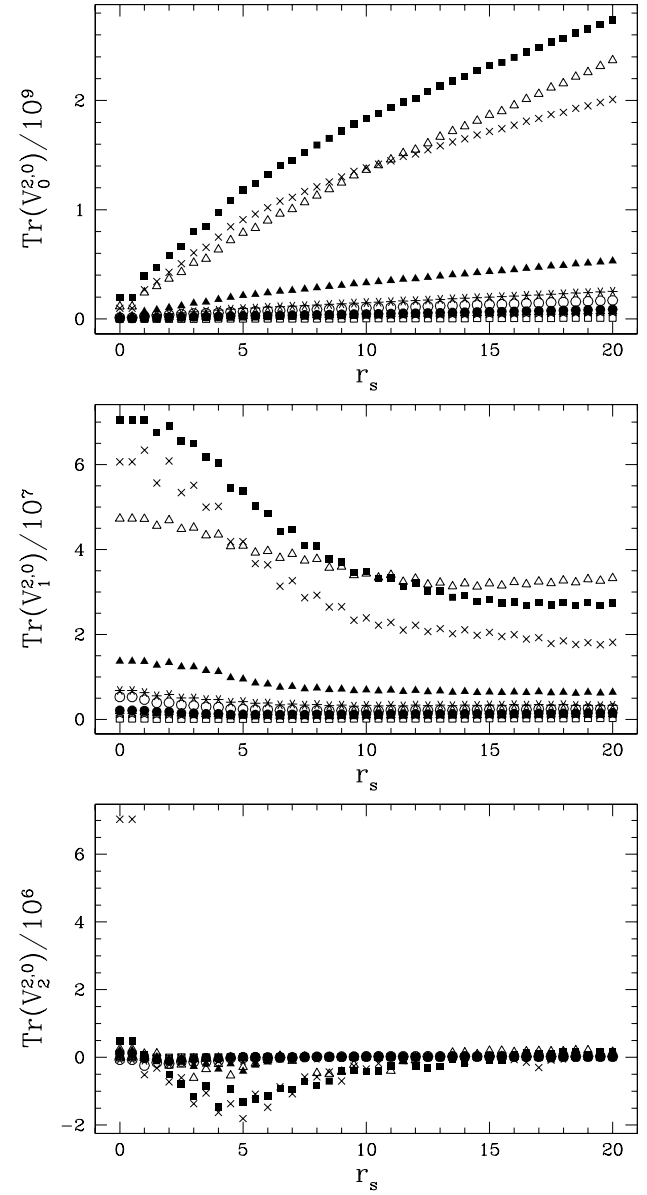


Fig. 14. The traces of the tensors $V_i^{2,0}$ for $i = 0, \dots, 2$ as a function of the smoothing length.

size-independent morphological characteristics. In order to calculate them, we considered the interval $r_s \in [0, 20]$ and a spacing of 0.2.

Our first feature space is spanned by the mean of the anisotropy parameter derived from $V_0^{2,0}$, $\overline{\text{anis}}(V_0^{2,0})$, and the mean of the anisotropy parameter corresponding to $V_1^{2,0}$, $\overline{\text{anis}}(V_1^{2,0})$. It is shown in Figure 17(a). There appears to be some systematic correlation between both characteristics: cells with higher $\overline{\text{anis}}(V_0^{2,0})$ tend to have higher $\overline{\text{anis}}(V_1^{2,0})$ as well. Given the meaning of these characteristics, this should not come as a surprise, although it is in principle possible to have high anisotropy in $V_0^{2,0}$ and low anisotropy in $V_1^{2,0}$. Thus, for discriminat-

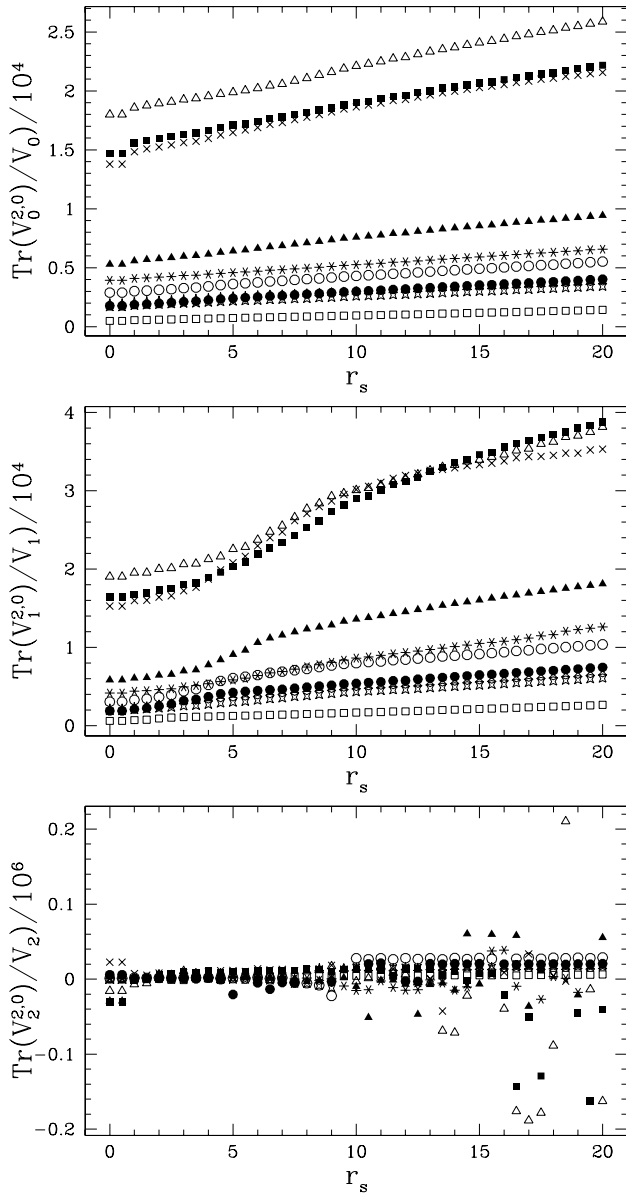


Fig. 15. The traces of $V_0^{2,0}$, $V_1^{2,0}$, and $V_2^{2,0}$, now normalized by the corresponding scalar V_0 , V_1 , or V_2 , respectively. If $V_2 = 0$ for some r_s , no data point is shown at all.

ing between different cells, one dimension of this feature space is essentially redundant. But the presence of some correlation might be used to describe some common trait shared by all cells.

A different situation can be observed for our second feature space. It is spanned by the monotonicity index i_s (dis₀) and by the half scale $h\left(\text{Tr}\left(V_1^{2,0}\right)\right)$. As can be seen from Figure 17(b), the scatter is larger, and the cells form kind of groups. Note, in particular, that neuronal cells that look similar at least in some respect tend to appear close to each other in this scatter plot. For instance, cells β , η , θ and ζ are close to each other in the bottom panel of Figure 17, especially regarding the position of their center of mass

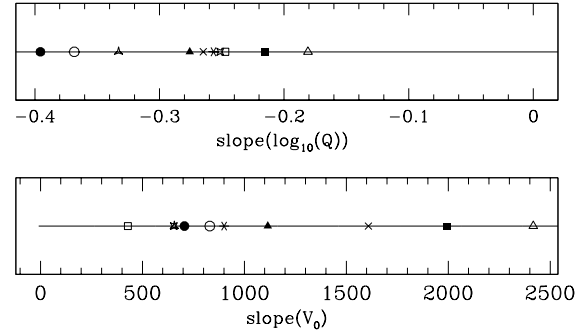


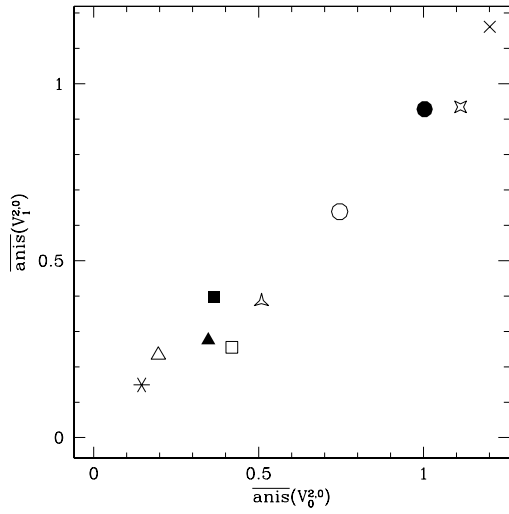
Fig. 16. The slopes of V_0 (top panel) and $\log_{10}(Q)$ for the different cells. The point styles are as above.

p_0 relatively to their soma. Figure 18 presents a dendrogram obtained by a simple hierarchical agglomerative clustering [35] of the scatter plot distribution shown in Figure 17(b). Such a structure suggests a possible *taxonomy* for the ten types of cells. As expected, the cells β , η , θ and ζ are similar, inhabiting the same branch at the lower part of the dendrogram. For the remaining subset, the cells α and κ end up markedly distinct from the group of cells formed by δ , ϵ , ι and λ .

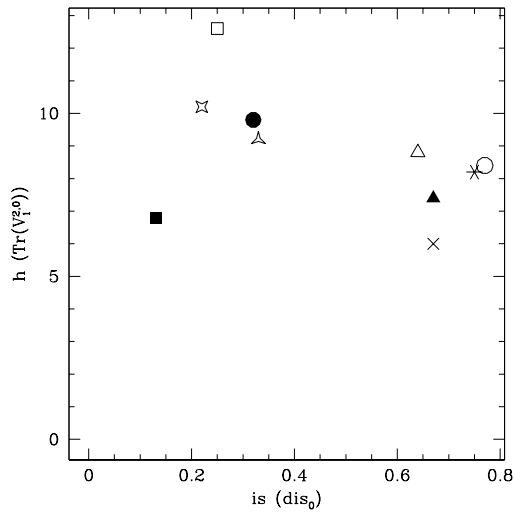
Although the proposed methodology may have a bearing on the classification of cat ganglion cells, it is difficult to make more definitive conclusions at this point, because the original classification [26] takes into account not only the neuronal morphology, but also the cell stratification and the size of the soma. Moreover, except for the more common α and β types, only a small number of examples of the cell types have been analyzed in the related literature [26]. A more detailed examination of which feature spaces are most useful has to wait for further data.

4 Conclusions

We have analyzed two-dimensional projections of neuronal cells using higher-order Minkowski valuations. Our measures detect different kinds of substructures, providing a natural extension of previous works that deal with the more traditional shape functionals [17,18]. An extensive discussion of the results obtained for a set of ten neuronal cells was included that illustrates the interpretation of the suggested measures and implications for neuromorphic studies. As far as our limited set of samples is concerned, significant similarities and differences between the cell types have been found, leading to a putative taxonomy. It is a pending question whether the differences found will still be characteristic of the types in a statistical sense.



(a)



(b)

Fig. 17. Scatter plots from selected features of an extended Minkowski analysis showing the population of the feature space with the neuronal cells.

This work was financially supported by FAPESP (processes 02/02504-01 and 99/12765-2) and CNPq (process 308231/03-1). It was also supported by the "Sonderforschungsbereich 375-95 fr Astro-Teilchenphysik" der Deutschen Forschungsgemeinschaft. C.B. thanks the Alexander von Humboldt Foundation, the German Federal Ministry of Education and Research and the Program for the Investment in the Future (ZIP) of the German Government for supporting this research. He also thanks Jens Schmalzing for providing software on which parts of the codes for this paper are built upon.

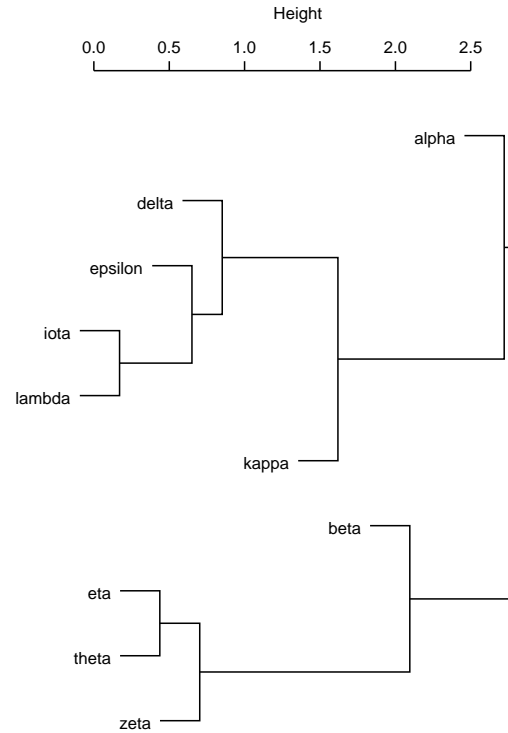


Fig. 18. The classification pattern according to an agglomerative hierarchical clustering analysis considering the two features selected for the scatter plot in Figure 17(b).

References

1. S. Douady and Y. Couder. *Physical Review Letters*, 68:2098–2101, 1992.
2. L. da F. Costa and E. T. M. Manoel. *Neuroinformatics*, 1(1):65–80, 2003.
3. H. Wässle, B. B. Boycott, and R. B. Illing. *Phil. Trans. R. Soc.*, 212:177–195, 1981.
4. Y. Fukuda, C. F. Hsiao, M. Watanabe, and H. Ito. *J. Neurophysiol.*, 52:999–1013, 1984.
5. Arjen van Ooyen, Jacob Duijnhouwer, Michiel W H Remme, and Jaap van Pelt. *Network: Comput. Neural Syst.*, 13:311–325, 2002.
6. L. da F. Costa and T. J. Velte. *Journal of Comparative Neurology*, 404(1):33–51, 1999.
7. G. A. Ascoli and J. L. Krichmar. *Neurocomputing*, 48(32–33):1003:1011, 2000.
8. R. C. Coelho and L. da F. Costa. *Neurocomputing*, 48(1–4):555–571, 2001.
9. S. Peng, B. Urbanc, L. Cruz, B. T. Hyman, and H. E. Stanley. *Proc. Nat. Ac. Sci.*, 100(7):3847–3852, 2003.
10. F. Rieke, D. Warland, R. de Ruyter van Steveninck, and W. Bialek. *Spikes: Exploring the Neural Code*. Bradford Books, 1999.
11. K. Morigiwa, M. Tauchi, and Y. Fukuda. *Neurosci. Res.*, 10:S131–9, 1989.
12. Regina Célia Coelho and L. da F. Costa. *Applied Signal Processing*, 3:163–176, 1996.

13. L. da F Costa, E. T. M. Manoel, F. Faucereau, J. Chelly, J. van Pelt, and G. Ramakers. *Network: Comput. Neural Syst.*, 13:283–310, 2002.
14. T. G. Smith, G. D. Lange, and W. B. Marks. *J. Neuroci. Methods*, 69:133, 1996.
15. E. P. Rodrigues, M. S. Barbosa, and L. da F. Costa. *Physical Review E*, Jun 2004.
16. R. M. Cesar and L. da F. Costa. *Biological Cybernetics*, 79(4):347–360, 1998.
17. M. S. Barbosa, E. S. Bernardes, and L. da F. Costa. *Physical Review E*, 67(061910), 2003.
18. M. S. Barbosa, L. da F. Costa, et al. *European Physical Journal B*, 37:109–115, 2003.
19. K. Michelsen and H. de Raedt. *Physics Report*, 347:461–538, 2001.
20. S. Alesker. *Geom. Dedicata*, 74:241, 1999.
21. R. Schneider. *Rend. Circ. Mat.*, Ser II, Suppl. 65:355, 2000.
22. R. Schneider and R. Schuster. *Rend. Circ. Mat.*, Ser II, Suppl. 70:295, 2002.
23. C. Beisbart, R. Dahlke, K. Mecke, and H. Wagner. *Vector- and tensor-valued descriptors for spatial patterns*, volume 600 of *Lecture Notes in Physics*, pages 238–260. Springer, 2002. arXiv:physics/0203072.
24. C. Beisbart, Thomas Buchert, and Herbert Wagner. *Physica A*, 293:592–604, 2001.
25. R. H. Masland. *Nature Neuroscience*, 4(9):877–886, 2001.
26. B. J. O’Brien, T. Isayama, R. Richardson, and D. M. Berson. *Journal of Physiology*, 538.3:787–802, 2002.
27. H. Hadwiger. *Vorlesungen über Inhalt, Oberfläche und Isoperimetrie*. Springer Verlag, Berlin, 1957.
28. W. Weil. Stereology: A survey for geometers. In Peter M. Gruber and Jörg M. Wills, editors, *Convexity and its applications*, pages 360–412. Birkhäuser, Basel, 1983.
29. S. Alesker. *Ann. of Math.*, 149 (3):977, 1999.
30. H. Hadwiger and C. Meier. *Mathematische Nachrichten*, 56:361, 1974.
31. Claus Beisbart and Klaus Mecke. Minkowski tensors. Unpublished Manuscript 2005.
32. D. Fenchel. *C.R. Acad. Sci. Paris*, 203:647, 1936. In French.
33. A. D. Alexandrov. *Matem. Sb. SSSR*, 2:1205–1238, 1937. In Russian, summary in German.
34. J. Schmalzing, T. Buchert, A. L. Melott, V. Sahni, B. S. Sathyaprakash, and S. F. Shandarin. *ApJ*, 526:568, 1999.
35. L. Kaufman and P. J. Rousseeuw. *Finding Groups in Data: An Introduction to Cluster Analysis*. Wiley-Interscience; 2nd Edition, 2005.